Inverse estimation of empirical parameters used in a regional ocean circulation model

Hirose, Naoki
Research Institute for Applied Mechanics, Kyushu University

出版情報：Journal of Oceanography. 67 (3), pp.323-326, 2011-06-01. Springer Japan
バージョン：

Inverse estimation of empirical parameters used in a regional ocean circulation model

Naoki HIROSE

Research Institute for Applied Mechanics, Kyushu University

Kasuga, Fukuoka 816-8580, Japan

E-mail: hirose@riam.kyushu-u.ac.jp

Submitted November 7, 2010

Revised December 25, 2010

Revised May 1, 2010

Keywords: parameter estimation, Green's function, surface momentum flux, river discharge, ocean circulation, East Asian marginal seas

Abstract

Significant impacts of the subgridscale parameterizations have been emphasized in modeling the ocean circulations, but various different parameter values are applied to similar numerical studies often without any justification. This study objectively estimates a set of empirical parameters along with their uncertainty for circulation modeling of the East Asian Marginal Seas. The solutions for 14 major parameters are obtained by using model Green's functions with constraints of climatological temperature and salinity data. The largest cost function reduction occurs in the eastern Japan Sea associated with the sharp gradient of the Polar Front. The calibrated parameters are also validated with realistic transport and path of Kuroshio in the final experiment. The inverse estimation shows that freshwater discharges from small rivers can be attributed to the coastal precipitation over a strip of land with 74–81 km wide. The thickness diffusion coefficient may be similar to the isopycnal and horizontal diffusion coefficients in their magnitude. The accelerated initial condition also contributes to the cost function reduction resulting in weaker trends of deep temperature. Most importantly, estimated scaling factors suggest a significant reduction of the reanalyzed wind stress data for more realistic ocean circulations. Possible reasons for the momentum missing are also discussed.

1. Introduction

The subgridscale parameterization is a crucial part of geophysical fluid modeling. Since the initial state of a model less influences the numerical solutions at longer-term integration, the fine-scale parameterizations can be relatively more important to the accuracy of climatic simulations. Even if their forms are physically-reasonable, inadequate configuration of the parameter values may cause significant bias in the numerical solutions. Thus the values of major parameters such as friction or mixing coefficients must be carefully selected.

However, the accuracy of empirical parameters used in ocean circulation models has been poorly known or discussed only partly. For instance, a large number of modeling studies have never examined parameter errors as if their uncertainty does not affect deterministic conclusions derived from a single set of parameters. The appropriate choice has been difficult yet due to mutual dependence of the parameters.

There may be two opposite approaches to determine the appropriate parameterizations. One is a physical or deductive method based on theoretical considerations or detailed modeling experiments. For instance, direct numerical simulation and large-eddy simulation dealing the subgridscale parameterizations for large-scale models belong to this category. Noh et al. (2004) performed a large-eddy simulation for the parameterization of surface mixing processes. The wave breaking and Langmuir circulation were found to contribute the vertical mixing considerably, which implies that the downward momentum flux is affected by the near-surface turbulent processes. The wave-current interaction may also modify the mean circulation, as deductively modeled by Rascle et al. (2006). Such a momentum distribution downward from the ocean surface is one of the most important subjects discussed in the present paper.

The other category involves statistical or inductive estimation based on a comparison with observational evidences. The inverse problems of parameter estimation may be specifically solved by adding the uncertain parameters to the state vector as adaptive or two-stage filtering (e.g., Dee and da Silva, 1998; Annan et al., 2005). Since the parameter estimation can be understood as a bias correction, unrealistic parameter values may affect the unbiased error statistics commonly assumed for optimal data assimilation methods such as the Kalman filtering. Some iterative methods based on four-dimensional variational formulation can also be powerful tools to optimize a large number of the parameters (e.g., Tziperman and Thacker, 1989; Navon, 1997; Evensen et al., 1998). However, these methods are often technically demanding and computationally expensive.

The present study aims to determine an optimal set of empirical parameters by a direct solver using model Green's functions following the study of Menemenlis et al. (2005). They suggested constructing the response matrix or the Green's functions numerically from the results of sensitivity experiments. Such an implementation

is much easier than the four-dimensional variational method or the Kalman filtering/smoothing. The inverse solutions with the Green's functions are given by linear, least-squares sense but still robust against nonlinearities and even provide the posteriori uncertainty (Menemenlis et al., 2005).

This study will examine an applicability of the Green's function approach to a high-resolution model by limiting the study region to the East Asian marginal seas and their surrounding area. Strong attentions are paid to the East China Sea (ECS) and the Japan Sea (JS) taking their advantages of wealthy dynamical features from coastal to deep circulations driven by complex forcing of wind, heat, freshwater, tide, and so on. Although the strong nonlinearity in the shallow waters might limit the linear inverse estimations, successful estimates of empirical parameters should give an important reference to the global ocean modeling at eddying regime since the calculation of their Green's functions is still costly.

This paper is organized as follows. The observational constraint is described in Section 2. Section 3 shows how the regional circulation model is constructed and also discusses the strong dependence of the results on the wind stress magnitude. Section 4 outlines how the selected parameters are optimized by Green's functions. The last section covers the conclusions and discussion.

2. Data constraint

The present optimization problem is constrained by climatological data of temperature and salinity in the East China Sea (ECS) and the Japan Sea (JS). The individual measurement data of temperature and salinity profile were averaged at each $1°\times1°$ box, standard depth, and climatological month by the Japan Oceanographic Data Center (JODC). The mean values (T^O, S^O) and their standard deviations (σ_T, σ_S) were obtained from the JODC website. In this study, the error variances (R^T, R^S) are assumed to be the same as the data variance at each cell (σ_T^2, σ_S^2) with lowest limits of $(0.5°\mathrm{C})^2$ and $(0.1\mathrm{PSU})^2$, respectively. It is noted that the prior error covariance accounts not only for the measurement errors but also for unresolved physics or representation errors of the model. For computational simplicity, the constraining data are limited to five depth levels (10, 30, 100, 300 and 1000m) and also to four climatological months (February, May, August, and November) resulting in a total of 3839 data values. This constraint covers well the dominant seasonal variation near the surface in the mid-latitude ocean basically. But the data constraint is expected to be weak at the Yellow Sea (YS) and also at the deep layers due to the small number of the measurement data.

The cost function is defined as

$$J = \sum_{i,j,k,t} \frac{\left(T^O_{i,j,k,t} - T^M_{i,j,k,t}\right)^2}{R^T_{i,j,k,t}} + \sum_{i,j,k,t} \frac{\left(S^O_{i,j,k,t} - S^M_{i,j,k,t}\right)^2}{R^S_{i,j,k,t}} \qquad (1)$$

where T^M and S^M are the model's equivalents and the subscripts i, j, k, and t indicate spatial and temporal indices.

3. Preliminary experiment

3.1 Model configuration

In this study, a western North Pacific Ocean model with $1/4° \times 1/5°$ (~22.2km square at 37°N) grid spacing is constructed on the basis of the RIAM Ocean Model framework, which is a primitive equation, hydrostatic, z-coordinate ocean general circulation model on a spherical coordinate with Arakawa B discretization (Lee et al., 2003). The calculation area extends from 105 to 180°E longitudinally and from 15 to 63°N latitudinally. However, the main focus of this study is the East Asian marginal seas and their surrounding area shown in Fig. 1. The open boundary and initial conditions are taken from the simulated result of a 1/6° Pacific Ocean model (You and Yoon, 2004) with a calibration of time-mean temperature and salinity using the JODC climatology for December and January. The prognostic variables are relaxed to the external model results near the eastern and southern boundaries to maintain the numerical stability. The external Pacific model has been run for 25 years by climatological monthly conditions, and the quasi-steady solutions are used for the initial and boundary conditions of this study.

[Fig. 1 is about here.]

The vertical thickness Δz is given in Fig. 2. The bottom cell allows a partial step (e.g., Pacanowski and Gnanadesikan, 1998). The surface mixing process is parameterized using the variable coefficients of the vertical diffusion and viscosity from the turbulent scheme of Noh and Kim (1999), which primarily accounts for the wave-induced mixing effect. A constant friction velocity associated with tidal variability gives an additional turbulent kinetic energy (TKE) into the deepest cells (~8.9×10^{-6} m^3/s^{-3}). The background vertical viscosity and diffusion coefficients are set to be $A_v = 10^{-4}\,m^2/s$ and $K_v = 10^{-5}\,m^2/s$. The bottom topography (Fig. 1) is similar to Hirose (2005) with some corrections and substitutions from the TaiDBM (Liu et al., 1998) and

ETOPO1 (National Geophysical Data Center, NGDC) data sets. The bottom drag is given by a quadratic form with a coefficient of 2.6×10^{-3}. No-slip and no-flux conditions are applied to the side boundary.

[Fig. 2 is about here.]

The surface meteorological conditions are given by daily-mean JRA-25 reanalysis data from 1979 to 1994. Every experiment in this study is performed for 18 years. The forcing of 1979–1980 is repeated twice to relieve the initial shock caused by the change from climatological to calendar forcings. The daily-mean forcing of 1981–1994 is succeeded from the four-year run. The analysis period is defined to be 12 years from 1983 to 1994 considering a climatic regime shift at 1988-1989. The long-term average may be more reliable by including multiple climate conditions.

The surface fluxes of momentum, precipitation, and long wave radiation are directly given to the top level of the model. The short wave radiation is distributed to the surface and subsurface layers due to its penetration. The sensible and latent fluxes at the neutral condition are calculated by a constant bulk transfer coefficient (1.35×10^{-3}) with a correction for the time-mean effect (Hanawa and Toba, 1987). An unstable/stable correction is also applied (Kondo, 1975). The fresh water flux from major rivers (Amur, Huanghe, and Changjiang) is given by the monthly mean data of the Global Runoff Data Centre (GRDC) and Senjyu et al. (2006). The discharge from minor rivers is assumed to be equivalent to the landward precipitation within 100km of the coastline, which is also calculated from the JRA-25 data.

The model's sea surface temperature (SST) is relaxed to the JRA-25 data with a time scale of 60 day, but there is no relaxation for the surface salinity. This ocean model does not include any explicit sea ice physics. Thus it assumes no upward heat fluxes, no downward turbulence input, and reduced wind stress at or below the freezing point (–1.8°C).

The lateral eddy diffusivity is parameterized by an isopycnal and thickness operators (Gent and McWilliams, 1990) with an additional Cartesian horizontal diffusion. Their coefficients are $K_i = 50\,\mathrm{m^2/s}$ and $K_e = K_h = 25\,\mathrm{m^2/s}$, respectively. The horizontal eddy viscosity is given by a combination of harmonic and biharmonic operators. These coefficients are assumed to be $A_h = 100\,\mathrm{m^2/s}$ and $A_b = 2\times10^{10}\,\mathrm{m^4/s}$, respectively. The horizontal viscosity and diffusion coefficients are close to the smallest level satisfying numerical stability.

Although I have carefully set up the numerical model, the present configuration still involves many

assumptions and empirical parameters similar to most ocean models to date. This study will minimize the uncertainty associated with the major parameters shown in Table 1 in the following sections.

[Table 1 is about here.]

3.2 Results

Figure 3(a) shows the 12-year mean sea surface height from the first experiment (Exp. A). The strong sea level gradient indicates the presence of a surface current such as the Kuroshio, Oyashio, or Tsushima Warm Current (TWC). The overall features of the current structure appeared to be reasonable, but a detailed analysis revealed some problems of this numerical solution.

[Fig. 3 is about here.]

First, the volume transport of the Kuroshio seems to be overestimated. For example, the eastward transport of Kuroshio across 137°E section of 31-34°N and 0-1000m depths reaches 56.0Sv, which is larger than the recent observations (e.g., Sugimoto et al., 2010). The stable undershooting path separated from Kii Peninsula of Fig. 3(a) may be attributed to the large volume transport of Kuroshio. Blocking anticyclone and cyclone are also found in the Kuroshio Extention region.

Since the Kuroshio is primarily driven by wind, the surface momentum flux over the model domain is uniformly reduced by 20% in the second experiment (Exp. B). The simulated transport at 137°E is decreased to an average of 48.1Sv, which is closer to the observational range. The time-mean path of the Kuroshio south of the Honshu Island also shifted northward as evidenced by the large positive difference of sea surface height in Fig. 3(b).

The northern cyclonic gyre of the JS in Exp. B is also weaker than that in Exp. A. A positive difference of the sea level at the central JS of Fig. 3(b) corresponds to the anticyclonic anomaly of Exp. B relative to Exp. A. In other words, the weaker cyclonic gyre allows more northward extension of the TWC in the central JS.

On the other hand, the volume transport of TWC hardly depends on the surface wind stress. The long-term mean transports through the Tsushima/Korea Strait are 2.5 and 2.4 Sv in Exp. A and B, respectively. They are already similar to an average of 2.5Sv for the 12-year analysis period calculated from sea level difference across

the Tsushima/Korea Strait by Nishimura et al. (2008). The weak dependence of the throughflow on the wind forcing might indicate relative importance of the other effects such as thermal or buoyancy forcing (e.g., Isoda, 1999).

Another difference is found in the YS. The 12-year mean temperature of Exp. B is 0.3-0.6°C lower than that of Exp. A at subsurface layers. The meridional heat transport with the YS Warm Current can be weaker in Exp. B than in Exp. A due to the reduced wind-driven circulations.

The simulated results are averaged for every month and 1°×1° box for more quantitative evaluation with the cost function (1). Experiment B actually shows ~7% improvement in the cost function over Exp. A (Table 1). A least-squares estimation of the best linear combination of the two experimental minimizing the cost function results shows an optimal solution of ~19% reduction of the wind stress data. It means that Exp. B is very close to the optimal case.

In the two experiments, the largest cost function values are found at the northeastern JS. The simulated temperature of Exp. A is significantly higher than the climatological data north of 40°N as shown in Fig. 4(a). The strong cyclonic circulation seems to carry excessive warm water from south to north along the Japanese coast. The reduced wind stress for Exp. B results in the colder temperature as evidenced by the 2°C contour near the Primorsky coast (Fig. 4b). The slower current seems to allow more heat loss to the atmosphere from the surface of the southern JS. The lower temperature contributes to the smaller cost function of Exp. B certainly.

Since the regional ocean circulations can also be affected by remote forcings, barotropic velocity at the eastern and southern open boundaries is reduced by 20% in Exp. B'. However, the transport of Kuroshio at 137°E is decreased from Exp. B by 0.8% only. The cost function also stays close to Exp. B (Table 1). The circulations of the study region seem to be nearly independent from the wind forcing out of the model domain. A tentative conclusion from the comparative experiments in this section is that the surface momentum flux data over the northwestern Pacific can be reduced to a certain degree for more realistic simulation of the circulations of the marginal seas and its vicinity.

[Fig. 4 is about here.]

4. Parameter estimation

4.1 Sensitivity experiment

The surface wind stress basically drives the ocean circulations and the mechanical energy is eventually dissipated by subgridscale processes. The preliminary results of the reduced wind stress imply the presence of near-surface, unresolved physics dissipating the mechanical energy. However, the momentum dissipation also occurs in bottom boundary processes in addition to the surface ones. The inverse estimation of surface momentum flux can not be closed without estimating the bottom flux. Furthermore the magnitude of each dissipation process can not be determined independently because they depend on each other.

This study inversely estimates the major empirical parameters shown in Table 1 by using model Green's functions following to Menemenlis et al. (2005). A series of sensitivity experiments are performed to derive the Green's function matrix $\mathbf{G}$, which is also known as response operator or data kernel.

The reference or baseline state is defined by Exp. B taking advantage of its smaller cost function than Exp. A. The sensitivity experiment on the wind stress (Exp. 1) is also taken from Exp. A as described in the previous section.

Experiments 2 and 3 are associated with the buoyancy forcing, which should influence the density structures followed by the mechanical motions. In the second experiment (Exp. 2), the bulk transfer coefficient for sensible and latent heat flux is slightly increased from the baseline conditions. Thus the simulated temperature and salinity near the surface is slightly lower and higher than the baseline experiment for most of the study area including the YS and the ECS, respectively. However, an opposite response is found in the western JS as shown in Fig. 5; the surface and subsurface temperature of Exp. 2 is significantly higher than that of Exp. B with the highest difference of 2°C near 39°N, 135.5°E, and 160m depth. This warming is basically provided by the northward extension of the EKWC and the Polar Front. It is also found that the intensified turbulent heat flux induces stronger formation of the intermediate water at 300-500m depth (not shown). The southward subduction of the intermediate water seems to drive the northward extension of the subtropical water for the buoyancy balance. The result of Exp. 2 also shows the cost function ~8% lower than that of the baseline experiment (Table 1). The modeled temperature and salinity filed may be further improved by increasing the turbulent bulk coefficient since the least-squares analysis indicates that an optimal bulk coefficient (1.43×10^{-3}) larger than Exp. 2 reduces the cost function furthermore (Table 2).

[Fig. 5 is about here.]

[Table 2 is about here.]

An original parameter defining the amount of minor river discharge is examined in Exp. 3. The landward precipitation range is shortened by 15% and the cost function also decreases significantly (Table 1). The optimal precipitation area may be smaller than the initial value (100 km). A regression analysis using the results of Exps. B and 3 returns an optimal estimate of 62km indeed (Table 2).

The effect of the river discharge parameter is obvious in coastal regions such as bays, but an interesting difference is found in the JS again; A difference of salinity between Exps. B and 3 starting at the Korean coast is elongated eastward to the subsurface levels (Fig. 6). Note that the order of 0.01PSU difference is significant considering the homogeneity of the northern and deep JS. As the fresh water subduction is often characterized with low temperature, the amount of the local river discharge influences not only salinity but also temperature distribution. Actually the temperature cost function is also reduced from Exp. B to Exp. 3. However in the YS and the ECS, the cost function is insensitive to this parameter because the dominant discharges of Changjiang and Huanghe are already accurate and not altered during the sensitivity experiments.

[Fig. 6 is about here.]

The vertical mixing processes are examined in Exp. 4-6. Experiment 4 changes the turbulent mixing from the surface only but affecting both the vertical eddy viscosity and diffusivity profiles. In a formulation of turbulent mixing scheme (Noh and Kim, 1999), an empirical parameter α dependent on the Richardson number must be calibrated properly for the vertical transport of TKE (see their equation 17 or 18). The sensitivity experiments (Exp. B versus Exp. 4) suggest that a smaller α, which allows more vertical penetration of the TKE and accelerates the vertical mixing of momentum and tracers, improves the model's representation of the temperature and salinity fields near the surface. The background vertical viscosity is doubled in Exp. 5 but the least-squares analysis reveals that its impact is small in minimizing the cost function. On the other hand, the cost function is more sensitive to a small change of the background vertical diffusion coefficient (Exp. 6).

The following five experiments are associated with horizontal dissipation processes for momentum and tracers. The horizontal viscosity given by a combination of harmonic and biharmonic operators was modified in Exps. 7 and 8, but the cost function does not change much in either way. The three types of the lateral diffusion

coefficients (K_i , K_e , K_h) were also changed in Exps. 9, 10, and 11, respectively. The simulated results uncover that the enhanced thickness diffusion coefficient (K_e) greatly contributes to the cost function reduction (Tables 1 and 2). A significant cost function reduction is associated with the positive difference of temperature (Exp. 10 minus Exp. B) at the central JS (Fig. 7). The mesoscale variability is actually strong in this region and the warm eddies often migrate northward (e.g., Isoda, 1994), but they are not explicitly resolved by the present 22km-mesh circulation model. The eddy-diffusion effect seems to work properly with the larger coefficient of thickness diffusivity in Exp. 10.

[Fig. 7 is about here.]

However, the model's sensitivity to the thickness diffusion parameter (Exp. 10) resembles the response to the bulk transfer coefficient (Exp. 2). For example, the positive and negative anomalies of temperature at the western central and northeastern JS of Fig. 7, respectively, are similar to those in Fig. 5. Such a coherence structure makes the inverse problem difficult. Their difference can be rather recognized in the vertical structure; the response to the thickness diffusion coefficient is shallower than that to the turbulent bulk coefficient. Another opposite response is found in the path of Kuroshio south of Honshu Island.

The bottom friction and mixing effects are examined in Exps. 12 and 13. But their changes incluence the cost function only weakly (Table 1). The optimal coefficients are also found to be close to the original small values within 10% difference as shown in Table 2. The model's weaker dependence to the bottom friction and mixing parameters suggests that the bottom boundary processes are not likely to be the reason of the wind stress reduction.

It is noted that the stronger bottom mixing certainly affects the salinity distribution in the western ECS. It enhances the vertical mixing of the surface fresh water from Chinese rivers and the deep saline water from Kuroshio in Exp. 13. However, such an effect is hardly measured by the present cost function (1) due to the small number of data in this region.

The initial condition of You and Yoon (2004) with JODC data correction is replaced in the last sensitivity experiment. The new initial condition for Exp. 14 is diverted from the final state of the baseline experiment (Exp. B). One may recognize this change as an acceleration of the numerical integration.

Figure 8 shows the time-series of deep temperature averaged over the ECS and the Japan Sea. The Japan Sea is apparently colder (and fresher) than the ECS due to active convection in winter. It is also interesting to find the

high-frequency changes of the 1000m temperature in the ECS, which is probably affected by the mesoscale variability. The simulated potential temperature is close to and higher than the climatological averages in the ECS and JS (4.55 and 0.15°C), respectively. The baseline experiment shows 0.1–0.2°C increase of the potential temperature during the experimental period in both of the seas. Such a warming trend is relaxed in Exp. 14. The long-term integration may be an advantage for obtaining accurate solutions as indicated by the smaller cost function of Exp. 14 (Table 1). This study seeks an optimal combination of the two initial conditions in the following section.

[Fig. 8 is about here.]

4.2 Inverse estimation

The results from a series of experiments were then subsampled at the data location. The differences between the baseline and sensitivity experiments essentially provide the column vectors of the Green's function matrix $\mathbf{G}$. This matrix may be recognized as the convolution of measurement function $\mathbf{H}$ with model's state transition $\mathbf{M}$. The linear inversion method of Menemenlis et al. (2005) is applied in this study as:

$$\boldsymbol{\eta}_a = \mathbf{P}\mathbf{G}^T\mathbf{R}^{-1}\mathbf{y}^d \qquad (2)$$

where $\boldsymbol{\eta}_a$ is the inverse solution and $\mathbf{y}^d$ is the innovation given by the difference between the observation data and the baseline experiment. The uncertainty of the constraint data is given by a diagonal matrix $\mathbf{R}$ whose components R_T and R_S has already been estimated in the preceding section. Matrix $\mathbf{P}$ is a posterior error covariance, which is calculated by using the following equation:

$$\mathbf{P} = \left(\mathbf{Q}^{-1} + \mathbf{G}^{-T}\mathbf{R}^{-1}\mathbf{G}\right)^{-1} \qquad (3)$$

where $\mathbf{Q}$ is the uncertainty of the initial parameters. Because the number of data constraints is much larger than the number of control parameters in this application, the inverse solutions are nearly independent from the parameter uncertainty and safely derived with an assumption of $\mathbf{Q}^{-1} = 0$.

The inverse solutions for the 14 parameters are given in Table 2. The total cost function is expected to be 4017.93 or 81.9% of the baseline experiment. Also shown in the table are the simpler estimates obtained from linear regressions of the baseline simulation and the corresponding perturbation results. Some of the single interpolations give the estimates close to the inverse solutions of the Green's function method, but others differ quantitatively from the optimal solutions using multiple parameters, indicating the linear dependence between

the empirical parameters.

This comprehensive optimization of the major parameters clarified that the surface wind stress should be reduced from the JRA-25 data by ~18% with an uncertainty significantly smaller than the perturbation of the wind stress. This scaling factor is turned out to be close to the baseline experiment. At the same time, the momentum missing can not be explained by increasing bottom stress since the optimal bottom drag coefficient stays close to the initial value (within 5% difference). Thus the weakened momentum flux is a very robust conclusion since every perspective examined in this study reaches the similar result. Physical reasons for this reduction are discussed in the last section.

The surface buoyancy forcing conditions were also intensively modified by this multiple regression analysis. The calibrated bulk transfer coefficient is still larger than the initial value but much smaller than the single regression result (Table 2). The coherent responses of the bulk coefficient and the thickness diffusivity (Exps. 2 and 10) seem to affect each contribution to the comprehensive optimization.

The fresh water flux from the minor rivers was estimated to be equivalent to the precipitation in a range of 74–81 km landward from the coastlines, which provides a good reference to the coastal boundary condition because of its simplicity.

Among several dissipative coefficients for momentum and tracers, the thickness diffusion coefficient (K_e), which flattened the isopycnal surfaces, was the most important parameter contributing the present optimization. The other seven parameters give minor impacts on the cost function reduction. It is still noteworthy that the three values of the lateral diffusion coefficients (K_i, K_e, K_h) are approaching each other, implying that they are equally important.

The bottom mixing effect was decreased drastically by the multiple regression analysis, which requires further examination in the following section. The initial condition can be certainly accelerated but the period is estimated to be half of the single regression result. The weaker corrections of many parameters imply the coherence of model's response to these parameters.

4.3 Final experiment

The expected cost function reduction was 18.1% based on the optimal combination of the sensitivity results. A new experiment (Exp. C) is then performed with the calibrated parameters. The total cost function is actually reduced by 17.7% from the baseline experiment. The small difference between the expected cost function and

the actual experimental result (Exp. C) basically validates the linear analysis. The nonlinearity between the parameters can be very weak in the present inversion process.

Figure 9 shows the 12-year mean sea surface height of the new simulation providing several differences from the baseline experiment (Fig. 3a). The central height of the subtropical gyre is ~10cm lower than Exp. B indicating a smaller volume transport of Kuroshio. The volume transport of the Kuroshio through the 137°E section is now 47.1Sv, which is within the observational range (Sugimoto et al., 2010). The stable undershooting path is largely corrected in Exp. C. Another improvement is the northward extension of the Polar Front in the western Japan Sea and the Subarctic Front in the western North Pacific at around 38°N. The strong temperature gradient of the Polar Front at the eastern Japan Sea also looks more realistic at Exp. C in comparison with the climatological data in Fig. 4. The enhanced heat loss in the western basin ends up with the lower temperature of the TWC near the eastern boundary. The changes of the TWC flow pattern may affect the northern subpolar gyre shifted to the east. Actually, this structure greatly contributes to the cost function reduction.

[Fig. 9 is about here.]

Although the cost function reduction is relatively smaller in the ECS than that in the JS, a certain difference is found at the subsurface layer as shown in Fig. 10. The coastal low salinity water has mixed into 100m depth at the shelf or slope region in Exp. B but it is much weaker in Exp. C. The local cost function is also smaller here in the final experiment. The smaller input of the bottom TKE should correct the excessive vertical mixing in the shallow area.

[Fig. 10 is about here]

The simulated deep temperature is even more stable and close to the climatological average (4.55°C) in the ECS in the final experiment (Fig. 8). However, the bias and trend have been hardly corrected for the JS. The bottom temperature of the YS becomes colder in Exp. C than that in Exp. B (not shown). In addition to the wind stress reduction, increased bulk coefficient and decreased vertical mixing seem to contribute to more formation of the YS Bottom Cold Water.

5. Conclusions and discussion

The important parameters of a regional ocean model were inversely estimated by using the model Green's functions. The Green's function matrix was numerically derived from a series of sensitivity experiment. A large cost function reduction of 24% from the first to the final experiments promises the improvement of model's accuracy. The nonlinearity appears to be negligible in the present case since the results of the calibrated experiment (Exp. C) almost coincides with the ones expected from the linear estimation.

The cost function reduction largely owes to the four parameters of wind stress scaling, coastal precipitation range, thickness diffusivity, and initial condition. Each sensitivity experiment has already revealed the strong sensitivity of the cost function to these parameters. It is noted that the multiple regression analysis decreases each change compared to the separated single regressions probably because of their correlations each other. For instance, the similar responses of the model to the perturbations of the bulk transfer and the thickness diffusion coefficients recall the inaccuracy of single optimizations assuming independence between the parameters.

One more important parameter to note is the tidal mixing effect. The single regression indicates a small improvement by changing the bottom TKE input, but a large correction has been estimated by the multiple regression analysis. The decreased TKE input should be more accurate judging from the realistic result of the final experiment for the subsurface temperature and salinity field in the YS and the ECS.

The small changes of the other parameters might indicate their high accuracy at the initial configuration. For example, the calibrated bulk transfer coefficient is close to the initial value regardless of its strong influence to the cost function. The bulk coefficient has actually been updated in a prediction system for the JES (Hirose et al., 2007).

However, it is more plausible that the weak sensitivity of the cost function limits more accurate estimation of remaining parameters. Namely, there can be a controllability problem. Introducing some other constraints from different observation data and/or expanding the analysis region will bring more accurate estimates of these parameters.

It can be bothersome for ocean modelers to account for the river discharges at various scales and locations. This study suggests that the fresh water flux from minor rivers can be approximately accounted for by the coastal precipitation. This method might be regarded as a zero-order hydrological model. The optimal precipitation range landward from the coastline was estimated to be 74–81km. The large impact on the salinity and temperature distributions at subsurface levels of the JS indicates that the small river discharges (such as Tumen

River) play an important role as well as Amur River for the water mass formations.

The inverse estimation also shows that the coefficients of the isopycnal, thickness, and horizontal diffusion approach each other. The assumption of similar constants for the three coefficients frequently made by previous studies (e.g., Hirst and McDougall, 1996) may be validated by the present regression analysis.

An objective acceleration of the numerical integration was also accomplished in this study by interpolating the initial condition and a final state. The deep water temperature was stable and accurate for the ECS in the calibrated experiment. However, the warming bias and trend of the JS indicates the difficulty to control the deep water property by the 14 parameters chosen in this study. Some physics missing in the present ocean model, such as a sea ice parameterization, might be required for more realistic simulation of the deep water properties.

The most important conclusion of this study is the reduction of the reanalyzed wind stress for properly driving an ocean circulation model. The effective wind stress was estimated to be 80.7–83.5% of the JRA-25 data. The reduction rate is similar to the preliminary estimate at Section 3 but more reliable owing to the comprehensive inverse estimation from the forcing to the dissipation processes at Section 4. The weakning of the wind stress over the mid- and high-latitude oceans was also obtained by Menemenlis et al. (2005).

There are at least two major factors explaining this wind stress reduction; overestimation of the momentum flux and momentum dissipation unresolved by the present model. The author speculates either one is important as the following discussions.

First of all, the downward momentum flux of the JRA-25 reanalysis data is compared with the other reanalysis products of ERA (European Centre for Medium-Range Weather Forecasts 40 year reanalysis) and NCEP (National Centers for Environmental Prediction/National Center for Atmospheric Research) in Fig. 11. Their horizontal resolutions are different, as is true for the detailed structure. But the large-scale, time-mean magnitude of the momentum flux is found to be similar between the data sets. The dominant southeastward component of the time-mean stress is $0.033\,\mathrm{N/m^2}$ with the JRA-25 reanalysis data in the ECS and JS region, which is even smaller than the similar average of $0.038\,\mathrm{N/m^2}$ for the ERA-40 and NCEP reanalysis data. The reduced wind stress (Fig. 11d) is significantly smaller than any of the three products. The strong wind stress exceeding 0.05 $\mathrm{N/m^2}$ is hardly found in the scaled plot except for the regions near Taiwan and the southeast JS. The overestimation of surface momentum flux seems to be a common problem for the reanalysis products.

[Fig. 11 is about here.]

The excessive magnitude of the reanalyzed wind stress might be naturally attributed to the overestimation of the wind speed near the ocean surface. However, the reanalyzed wind speed is not likely to contain such a large bias because various wind data have been assimilated into atmospheric models and the reanalyzed estimates have been intensively validated with many in-situ measurements. It is more plausible to consider the errors in the wind stress data given a small number of direct measurements of the surface momentum flux.

To my best knowledge, all the reanalysis calculations neglected the surface current and wave speed contribution in the wind stress estimation. A common error in the surface momentum flux data can arise from the difference of the relative and absolute wind speed to the ocean surface. For example, Duhaut and Straub (2006) obtained an rms difference of 7% in the wind stress arising from the surface current effect using an idealized double gyre model. Since the surface currents and waves are usually correlated with the atmospheric wind near surface, an overall reduction in the wind stress magnitude is expected by considering the current and wave speed in the calculation of the wind stress. Kara et al. (2007) estimated ~10% reduction of the drag coefficient (C_D) by taking the effects of the surface currents and wave speeds into account. Eden and Dietze (2009) found a significant reduction of surface kinetic energy associated with mesoscale eddies by using the air-sea velocity difference. These studies support at least partly the estimated reduction of the present analysis.

The wind stress reduction may be caused not only by the data errors but also by physical reasons, especially unresolved physics of a finite resolution model. Perrie et al. (2003) showed that 20–30% of the surface momentum flux from the atmosphere was transferred to surface waves, whereas the remainder drove the surface current directly. However, they also concluded that a large part of this wave dissipation was eventually converted to the surface current through the wave-current interactions. The reduction rate of the downward flux due to the surface wave variability is probably around 5–6% as explained by Mitsuyasu (1985).

One more possibility is a dissipation of momentum due to internal wave drag. Previous studies already clarified that the rapid tidal motions caused the momentum loss associated with internal wave breaking (e.g., Jayne and St. Laurent, 2001). Hirose et al. (2001) also implied the similar effect in the wind-driven motions by showing a consistency between the effective friction parameter and the roughness of the bottom topography. The present inverse solution might be calling for an ocean analogue to the gravity wave drag parameterization in atmospheric circulation models.

Acknowledgements

The author wishes to thank Naoto Ebuchi (Hokkaido University), Akira Masuda, Katsuto Uehara (Kyushu University), Yign Noh (Yonsei University), Yu-heng Tseng (National Taiwan University), Victor Zlotnicki and Lee-Leung Fu (Jet Propulsion Laboratory) for their valuable comments and suggestions on this study. The author would also like to thank the Japan Oceanographic Data Center (JODC), Global Runoff Data Centre (GRDC), and National Geophysical Data Center (NGDC) for providing useful datasets. Many drawings were made with Grid Analysis and Display System (GrADS). This study was a part of Data assimilation Research of the East Asian Marine System (DREAMS) project supported by Grant-in-Aid for Scientific Research and also by Research and Development Projects for Application in Promoting New Policy of Agriculture Forestry and Fisheries, Japan.

References

[1] Annan, J. D., J. C. Hargreaves, N. R. Edwards and R. Marsh (2005): Parameter estimation in an intermediate complexity earth system model using an ensemble Kalman filter. Ocean Modelling 8, 135–154.

[2] Dee, D. P. and A. M. da Silva (1998): Data assimilation in the presence of forecast bias. Q. J. R. Meteorological Soc. 124, 269–295.

[3] Duhaut, T. H. and D. N. Straub (2006): Wind stress dependence on ocean surface velocity: Implications for mechanical energy input to ocean circulation. J. Phys. Oceanogr. 36, 202–211.

[4] Eden, C. and H. Dietze (2009): Effects of mesoscale eddy/wind interactions on biological new production and eddy kinetic energy. *J. Geophys. Res.*, 114, C05023.

[5] Evensen, G., D. P. Dee and J. Schröter (1998): Parameter estimation in dynamical models. In: Chassignet, E. P., Verron, J. (Eds.), Ocean Modeling and Parameterization. Kluwer Academic, Netherlands, 373–398.

[6] Gent, P. R. and J. C. McWilliams (1990): Isopycnal mixing in ocean circulation models, J. Phys. Oceanogr. 20, 150–155.

[7] Hanawa, K. and Y. Toba (1987): Critical examination of estimation methods of long-term mean air-sea heat and momentum transfers. Ocean-Air Inter. 1, 79–93.

[8] Hirose, N., I. Fukumori, V. Zlotnicki and R. M. Ponte (2001): Modeling the high-frequency barotropic response of the ocean to atmospheric disturbances: Sensitivity to forcing, topography, and friction. J. Geophys. Res. 106, 30987–30995.

[9] Hirose, N. (2005): Least-squares estimation of bottom topography using horizontal velocity measurements in the Tsushima/Korea Straits. J. Oceanogr. 61, 789–794.

[10] Hirose, N., H. Kawamura, H. J. Lee, J.-H. Yoon (2007): Sequential forecasting of the surface and subsurface conditions in the Japan Sea. J. Oceanogr. 63, 467–481.

[11] Hirst, A. C. and T. J. McDougall (1996): Deep-water properties and surface buoyancy flux as simulated by a z-coordinate model including eddy-induced advection. J. Phys. Oceanogr. 26, 1320–1343.

[12] Isoda, Y. (1994): Warm eddy movement in the eastern Japan Sea. J. Oceanogr. 50, 1–15.

[13] Isoda, Y. (1999): Cooling-induced current in the upper ocean of the Japan Sea. J. Oceanogr. 55, 585–596.

[14] Jayne, S. R. and L. C. St. Laurent (2001): Parameterizing tidal dissipation over rough topography. Geophys. Res. Lett. 28. 811–814.

[15] Kara, A. B., E. J. Metzger and M. A. Bourassa (2007): Ocean current and wave effects on wind stress drag coefficient over the global ocean. Geophys. Res. Lett. 34, L01604.

[16] Kondo, J. (1975): Air-sea bulk transfer coefficients in diabatic conditions. Bound.-Layer Meteor. 9, 91–112.

[17] Lee, H. J., J.-H. Yoon, H. Kawamura and H.-W. Kang (2003): Comparison of RIAMOM and MOM in modeling the East Sea/Japan Sea circulation. Ocean Polar Res. 25, 287–302.

[18] Liu, C. S., S. Y. Liu, S. E. Lallemand, N. Lundberg and D. Reed (1998): Digital elevation model offshore Taiwan and its tectonic implications. Terrest. Atmos. Oceanic Sci. 9, 705–738.

[19] Menemenlis, D., I. Fukumori and T. Lee (2005): Using Green's fnctions to calibrate an ocean general circulation model. Mon. Weather Rev. 133, 1224−1240.

[20] Mitsuyasu, H. (1985): A note on the momentum transfer from wind to waves. J. of Geophys. Res. 90, 3343−3345.

[21] Nishimura, K., N. Hirose, K. Fukudome (2008): Long-term estimation of volume transport through the Tsushima Straits. Report of Res. Inst. Appl. Mech. 135, 113−118. (in Japanese with English abstract)

[22] Navon, I. M. (1997): Practical and theoretical aspects of adjoint parameter estimation and identifiability in meteorology and oceanography. Dyn. Atmos. Oceans 27, 55−79.

[23] Noh, Y. and H. J. Kim (1999): Simulations of temperature and turbulence structure of the oceanic boundary layer with the improved near-surface process. J. Geophys. Res. 104, 15621−15634.

[24] Noh, Y., H. S. Ming and S. Raasch (2004): Large eddy simulation of the ocean mixed layer: The effects of wave breaking and Langmuir circulation. J. Phys. Oceanogr. 34, 720−735.

[25] Pacanowski, R. and A. Gnanadesikan (1998): Transient response in a z-level ocean model that resolves topography with partial cells. 126, 3248−3270.

[26] Perrie, W., C. L. Tang, Y. Hu, B. M. DeTracy (2003): The impact of waves on surface currents. J. Phys. Oceanogr. 33, 2126−2140.

[27] Rascle, N., F. Ardhuin and E. A. Terray (2006): Drift and mixing under the ocean surface: A coherent one-dimensional description with application to unstratified conditions. J. Geophys. Res. 111, C03016.

[28] Senjyu, T., H. Enomoto, T. Matsuno and S. Matsui, (2006): Interannual salinity variations in the Tsushima Strait and its relation to the Changjiang discharge. J. Oceanogr. 62, 681−692.

[29] Sugimoto, S., K. Hanawa, K. Narikiyo, M. Fujimori and T. Suga, (2010): Temporal variations of the net Kuroshio transport and its relation to atmospheric variations. J. Oceanogr. 66, 611−619.

[30] Tziperman, E. and W. C. Thacker, (1989): An optimal-control/adjoint-equations approach to studying the

ocean general circulation. J. Phys. Oceanogr. 19, 1471−1485.

[31] You, S. H. and J.-H. Yoon (2004): Modeling of the Ryukyu Current along the Pacific side of the Ryukyu Island. Pacific Oceanogr. 2, 44−51.

Tables

Table 1. List of parameters controlled in this study with the total cost function of each experiment. All the default values are applied for the baseline experiment (Exp B). Experiment 1 is identical to Exp. A. Each perturbed value is used for each sensitivity experiment. The same bulk coefficient is applied for calculating the sensible and latent heat flux. The coastal precipitation range determines the amount of discharges from small rivers. The effect of stratification to the vertical diffusivity and viscosity is controlled by an empirical parameter α multiplied with the Richardson number (Ri) as Noh and Kim (1999). The horizontal viscosity in momentum equation is modeled by a combination of harmonic and biharmonic operators. The lateral diffusivity for tracers also integrates the three effects of isopycnal diffusion, thickness diffusion of isopycnal surface, and Cartesian horizontal diffusion. The turbulent kinetic energy (TKE) from the bottom models tidal mixing. The initial condition is basically given by the long-term integration result of You and Yoon (2004) but the final field of Exp. B is used for Exp. 14.

Experiment	Parameter	Default	Perturbed	Cost function
Baseline	(default values)	all	none	4903.37
B’	Barotropic velocity at open boundary [%]	100	80	4936.82
1 (A)	Scaling of wind stress [%]	80	100	5298.56
2	Bulk transfer coefficient [$\times 10^{-3}$]	1.35	1.40	4512.09
3	Coastal precipitation range [$\times 10^{3}$ m]	100	85	4668.77
4	TKE dependence on Ri (α)	120	115	4807.30
5	Background vertical viscosity [$\times 10^{-4}$ m^2/s]	1.0	2.0	4830.75
6	Background vertical diffusion [$\times 10^{-4}$ m^2/s]	0.1	0.09	4749.22
7	Biharmonic viscosity coef. [$\times 10^{8}$ m^4/s]	200	250	4819.11
8	Harmonic viscosity coef. [m^2/s]	100	80	4863.24
9	Isopycnal diffusion coef. [m^2/s]	50	100	4926.62
10	Thickness diffusion coef. [m^2/s]	25	30	4622.52
11	Horizontal diffusion coef. [m^2/s]	25	20	4876.38
12	Bottom drag coefficient [$\times 10^{-3}$]	2.6	2.5	5016.54
13	Bottom TKE input [$\times 10^{-6}$ m^3/s^{-3}]	8.944	12.500	4932.03
14	Initial condition [years since 1977]	0	18	4462.25

Table 2. Result of optimizations for a single parameter by linear interpolation and also for multiple parameters using model Green's functions

Parameter	Single		Multiple	
	Value	Cost function	Value	Error
1. Scaling of wind stress [%]	80.87	4902.55	82.12	±1.40
2. Bulk transfer coefficient [$\times 10^{-3}$]	1.4272	4456.75	1.3657	±0.0072
3. Coastal precipitation range [$\times 10^{3}$ m]	61.76	4531.38	77.62	±3.45
4. TKE dependence on Ri (α)	110.94	4783.18	114.04	±1.17
5. Background vertical viscosity [$\times 10^{-4}$ m^2/s]	2.354	4825.42	1.079	±0.250
6. Background vertical diffusion [$\times 10^{-4}$ m^2/s]	0.0814	4707.10	0.0968	±0.0025
7. Biharmonic viscosity coef. [$\times 10^{8}$ m^4/s]	290.70	4797.84	216.73	±13.89
8. Harmonic viscosity coef. [m^2/s]	79.41	4863.22	116.66	±5.07
9. Isopycnal diffusion coef. [m^2/s]	69.44	4887.61	44.51	±7.48
10. Thickness diffusion coef. [m^2/s]	36.90	4480.25	31.40	±1.03
11. Horizontal diffusion coef. [m^2/s]	20.81	4875.35	28.04	±1.12
12. Bottom drag coefficient [$\times 10^{-3}$]	2.688	4871.40	2.703	±0.020
13. Bottom TKE input [$\times 10^{-6}$ m^3/s^{-3}]	9.516	4902.29	0.640	±0.808
14. Initial condition [years since 1977]	24.68	4427.32	12.78	±1.87

Figure legend

Fig. 1. Area of interest with model topography. The contour interval is five vertical levels of the ocean model. Each number indicates corresponding depth (m). The abbreviations JS, YS, ECS, TKS, and CJ indicate the Japan Sea, Yellow Sea, East China Sea, Tsushima/Korea Strait, and Changjiang River mouth.

Fig. 2. Model's vertical thickness (Δz) as a function of its central depth [m].

Fig. 3. (a) Mean sea surface height simulated by Exp. A for the period from 1983 to 1994. The contour interval is 5cm. Dashed contour indicates negative. (b) Mean sea level difference between Exp. B and Exp. A. Shaded area indicates negative. Note uneven contour interval.

Fig. 4. Long-term mean temperature for August at 100m depth in the northeastern Japan Sea given by (a) Exp. A, (b) Exp. B, (c) Exp. C, and (d) JODC climatology, respectively.

Fig. 5. Difference of 12-year mean temperature at 30m depth between Exp. B and Exp. 2. The contour interval is 0.2°C. Shaded area indicates negative.

Fig. 6. Difference of Exp. B and Exp. 3 in long-term mean salinity at section of 39°N in the upper Japan Sea. The horizontal and vertical axes indicate longitude (°E) and depth (m), respectively. The contour interval is 0.1PSU.

Fig. 7. Difference of 12-year mean temperature at 30m depth between Exp. B and Exp. 10. The contour interval is 0.1°C. Shaded area indicates negative.

Fig. 8. Time series of potential temperature [°C] at 1000m depth averaged over (a) the East China Sea and (b) the Japan Sea for the simulation period. The thick, thin and dashed curves indicate the results of Exps. B, 14, and C, respectively.

Fig. 9. Same as Fig. 3(a) but for Exp. C.

Fig. 10. Long-term mean salinity distribution for November at 100m depth in the East China Sea by (a) Exp. B and (b) Exp. C. The contour interval is 0.1PSU. Shaded area indicates salinity lower than 34.5PSU.

Fig. 11. Time-mean surface wind stress of (a) ERA-40, (b) NCEP, (c) JRA-25, and (d) 80%-scaled JRA-25 over the ocean for the period from 1983 to 1994. The vector scale is indicated at ~44°N, 125°E. The light and dark shade shows the magnitude stronger than 0.025 and 0.05 N/m^2, respectively.

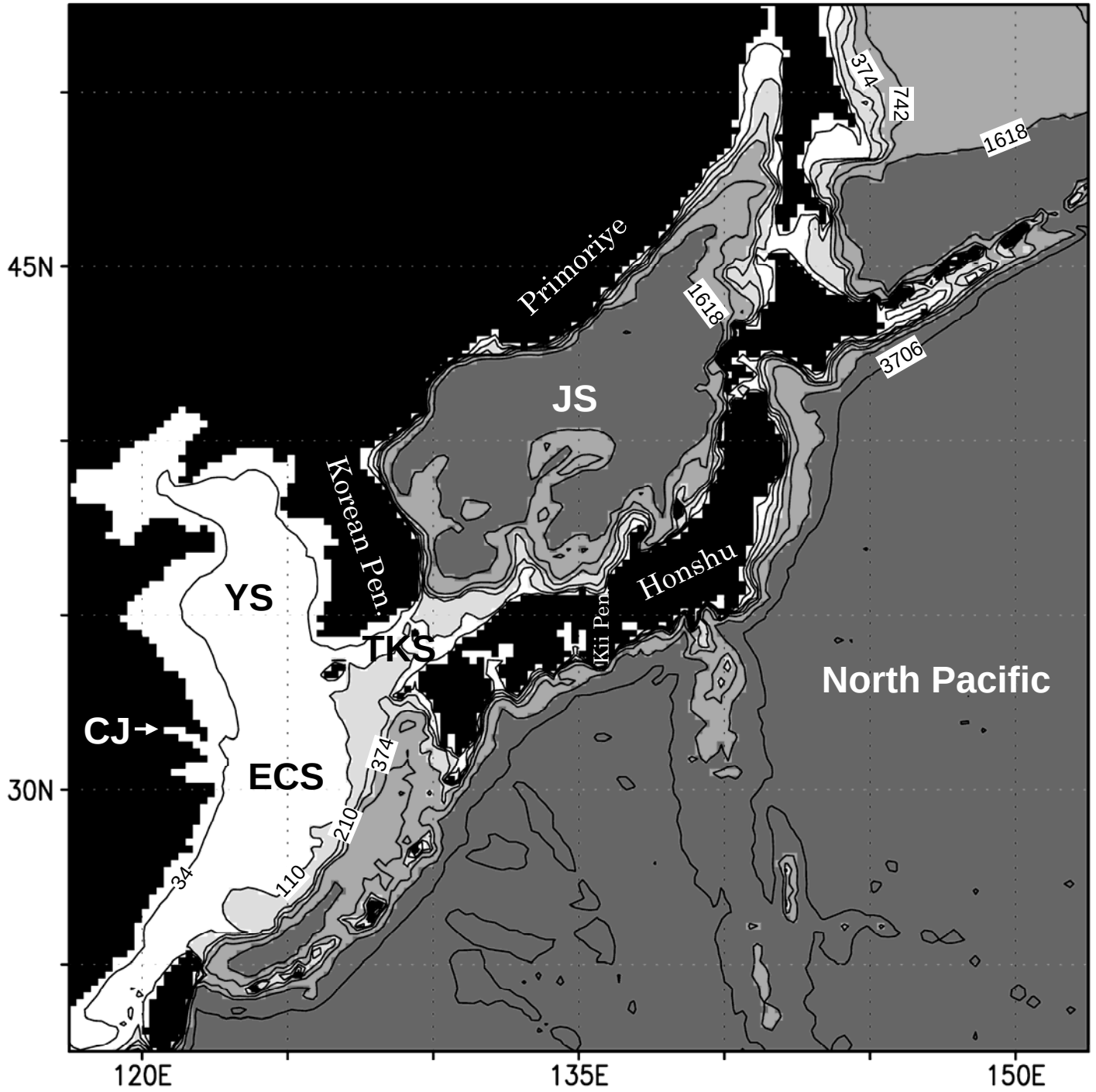
45N
30N
120E
135E
150E
Primoriye
Korean Pen.
Honshu
Kii Pen.
JS
YS
TKS
ECS
CJ
North Pacific
374
742
1618
1618
3706
374
210
110
34

Fig. 1

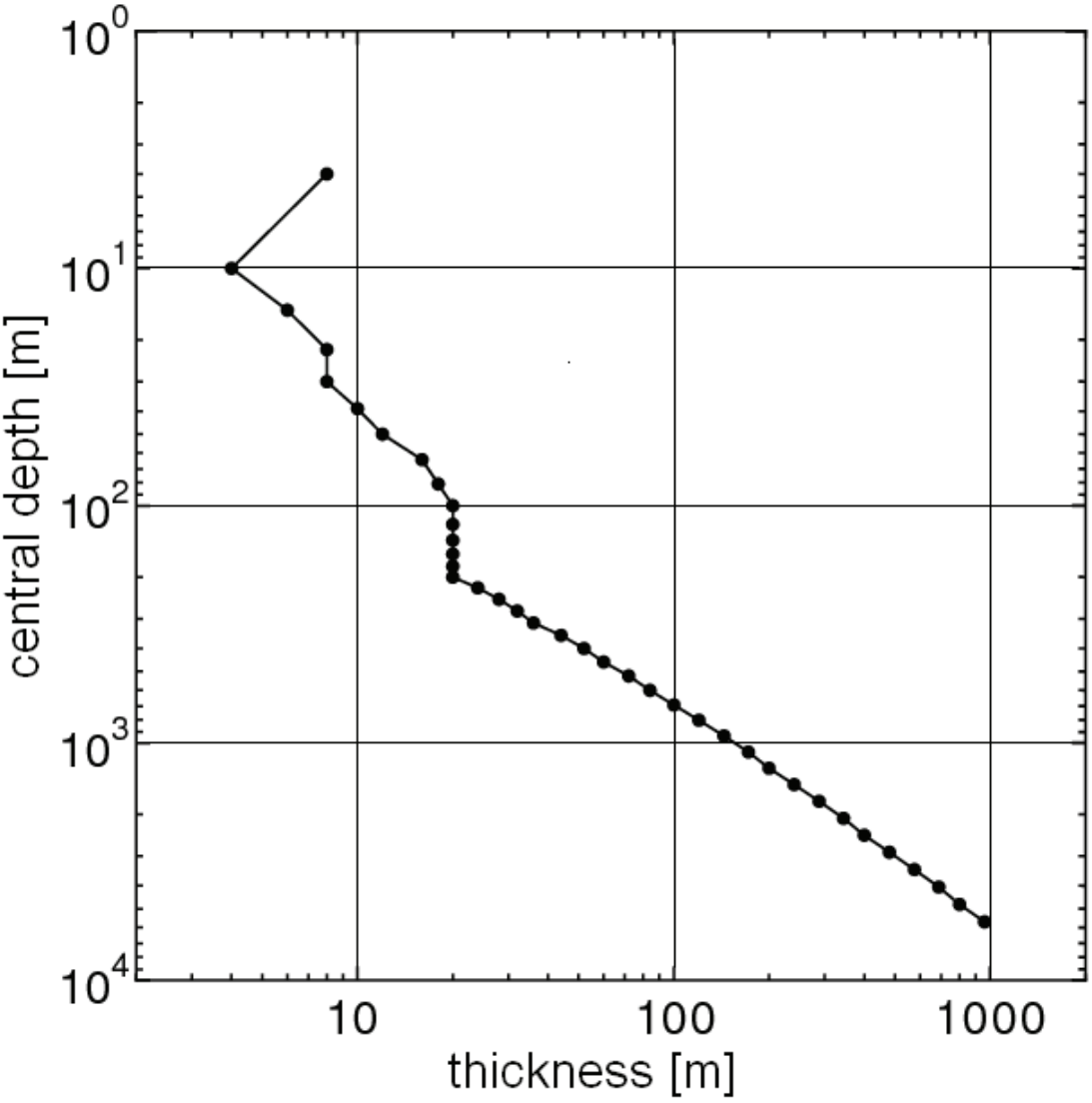

Fig. 2

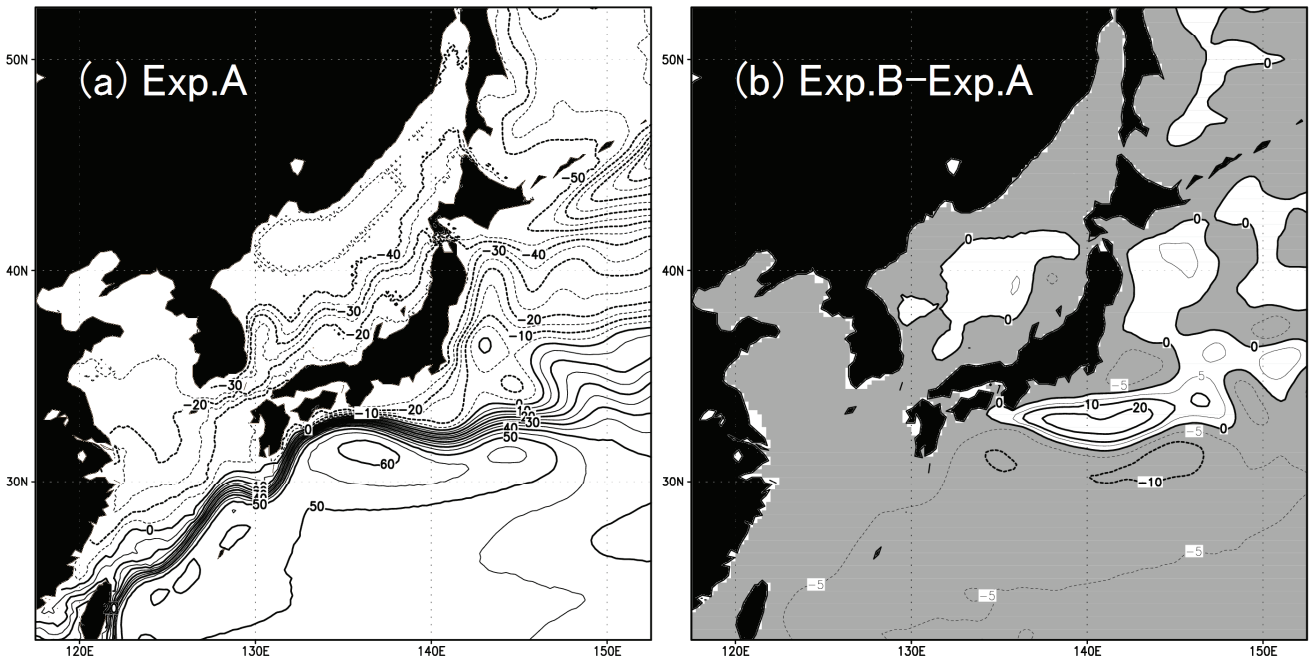

Fig. 3

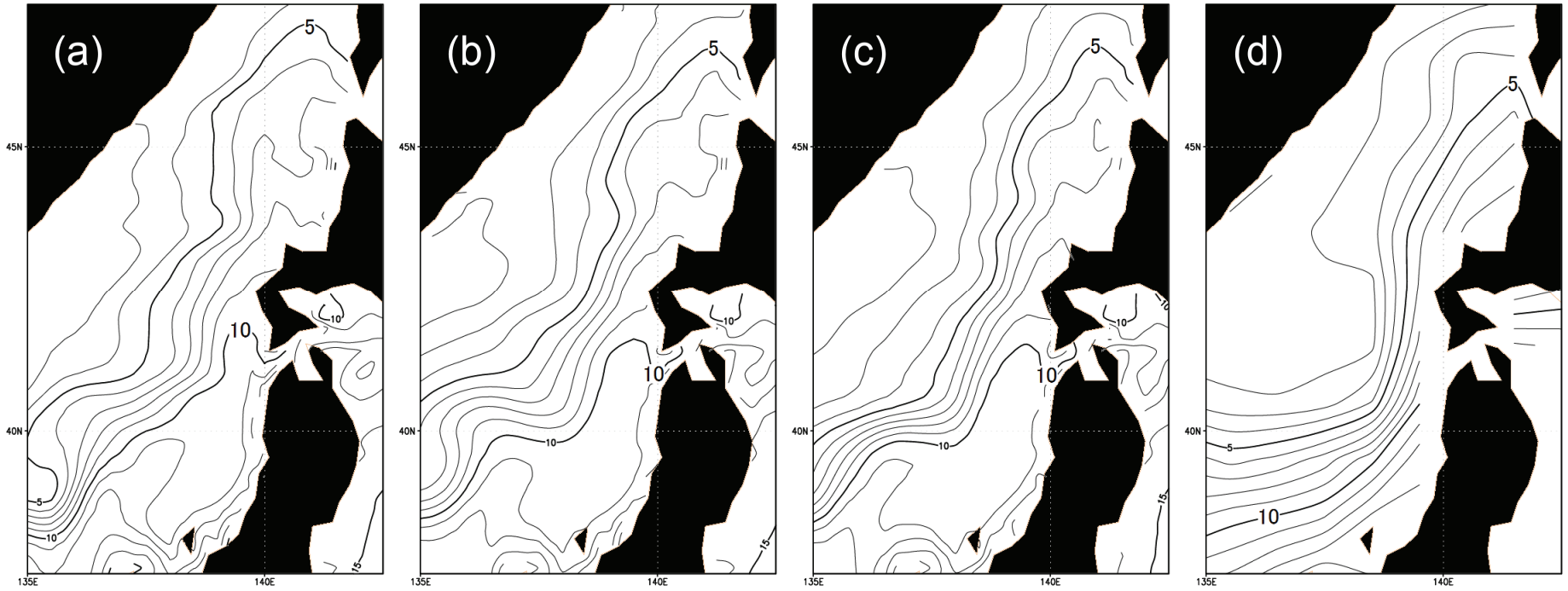

Fig. 4

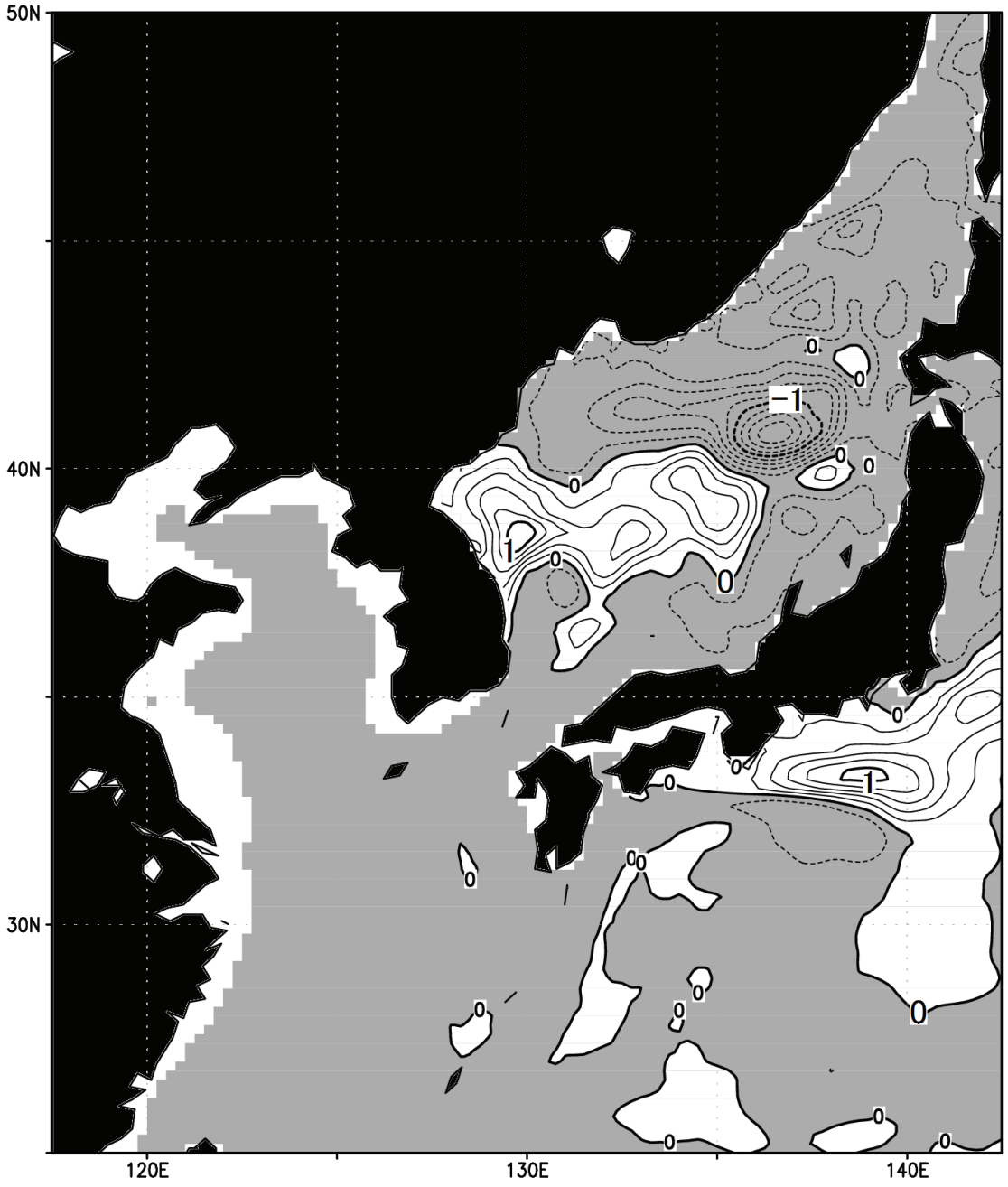

Fig. 5

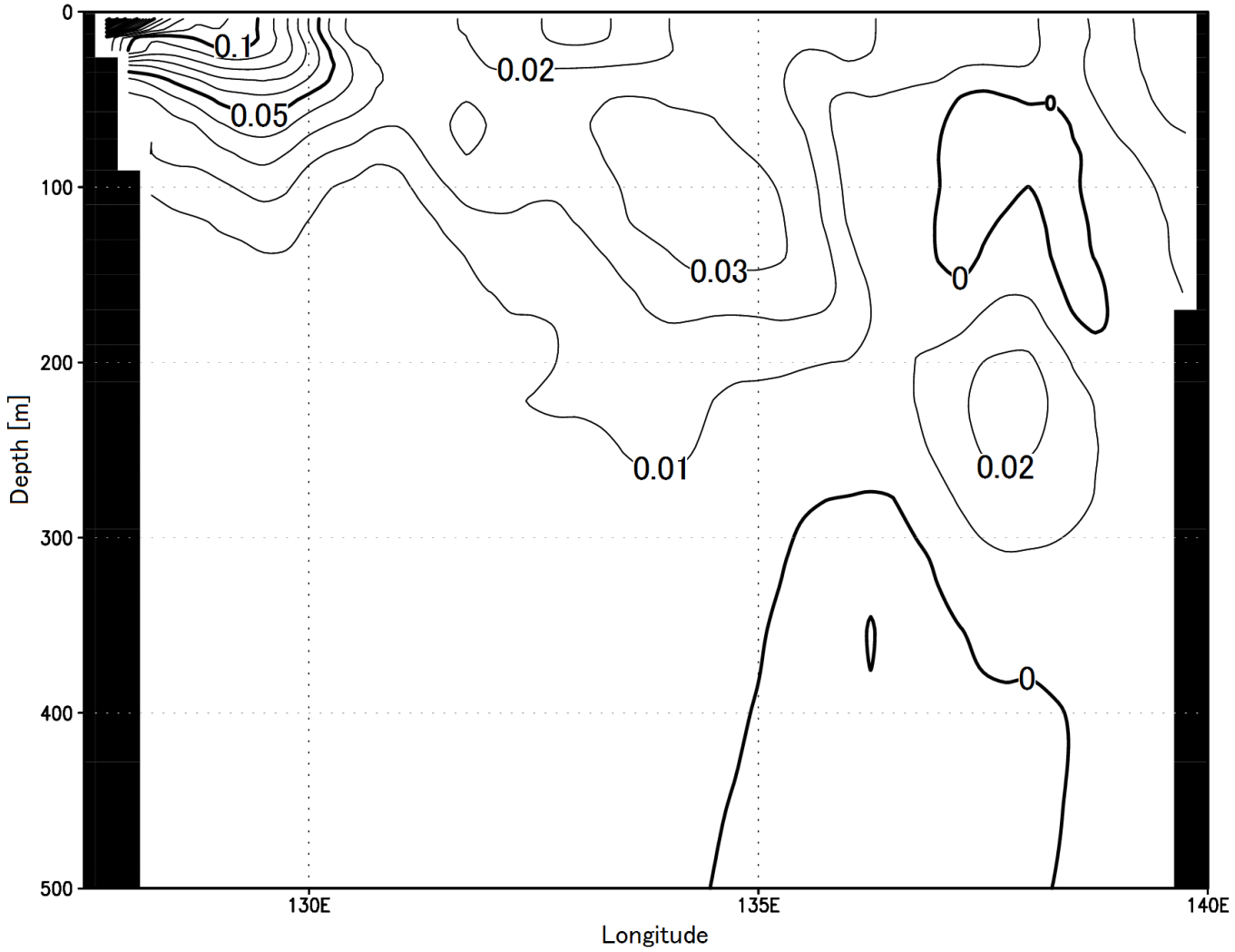
0
100
200
300
400
500
Depth [m]
0.1
0.05
0.02
0.03
0
0
0.01
0.02
0
130E
135E
140E
Longitude

Fig. 6

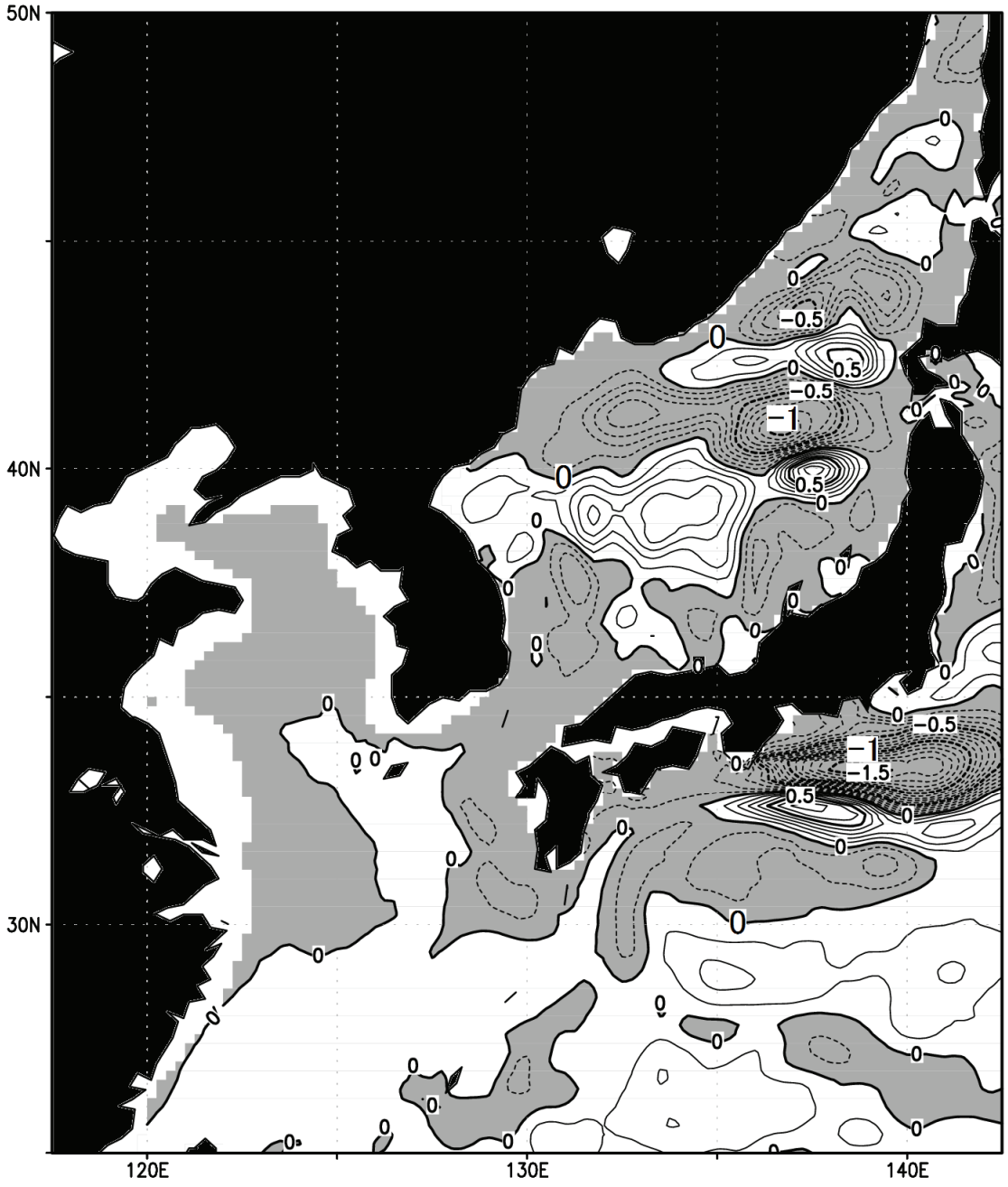

Fig. 7

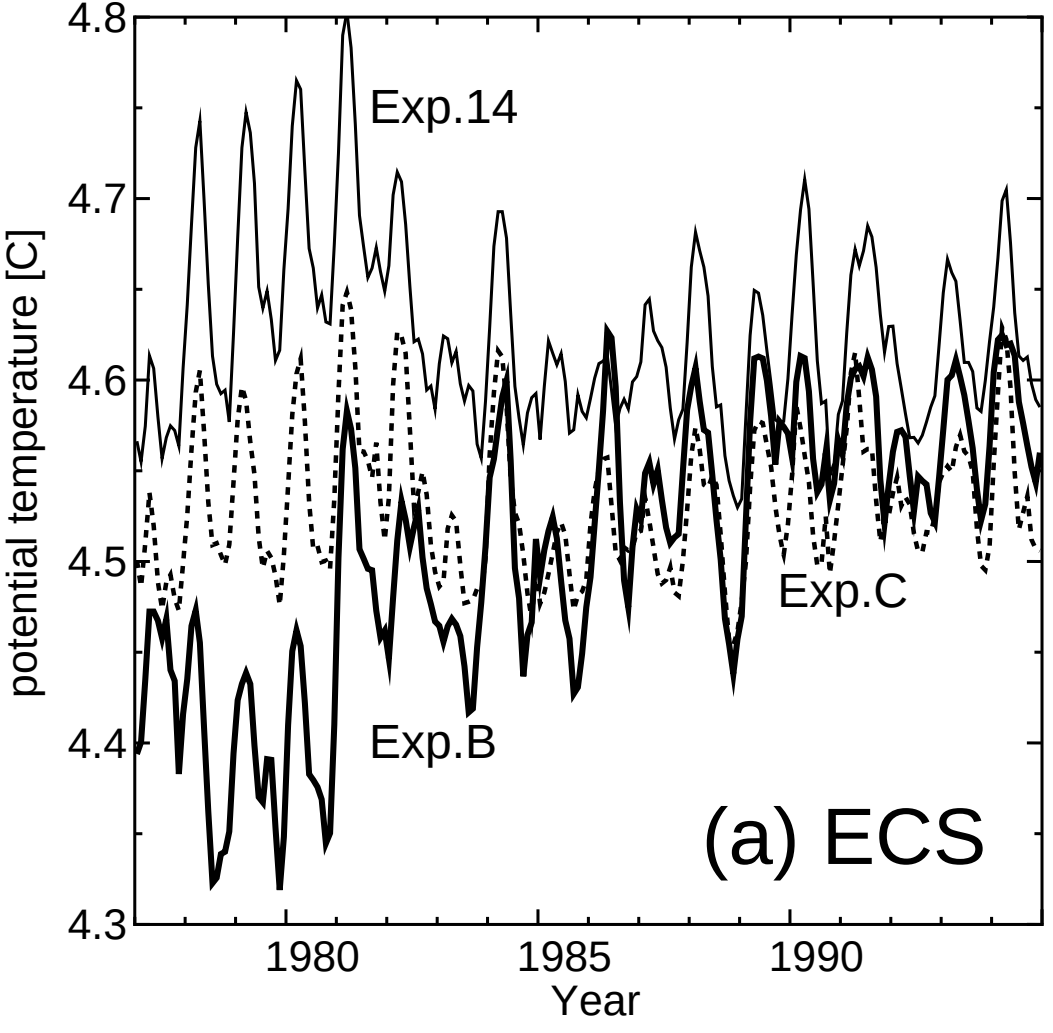
potential temperature [C]
4.8
4.7
4.6
4.5
4.4
4.3
Exp.14
Exp.C
Exp.B
(a) ECS
1980
1985
1990
Year

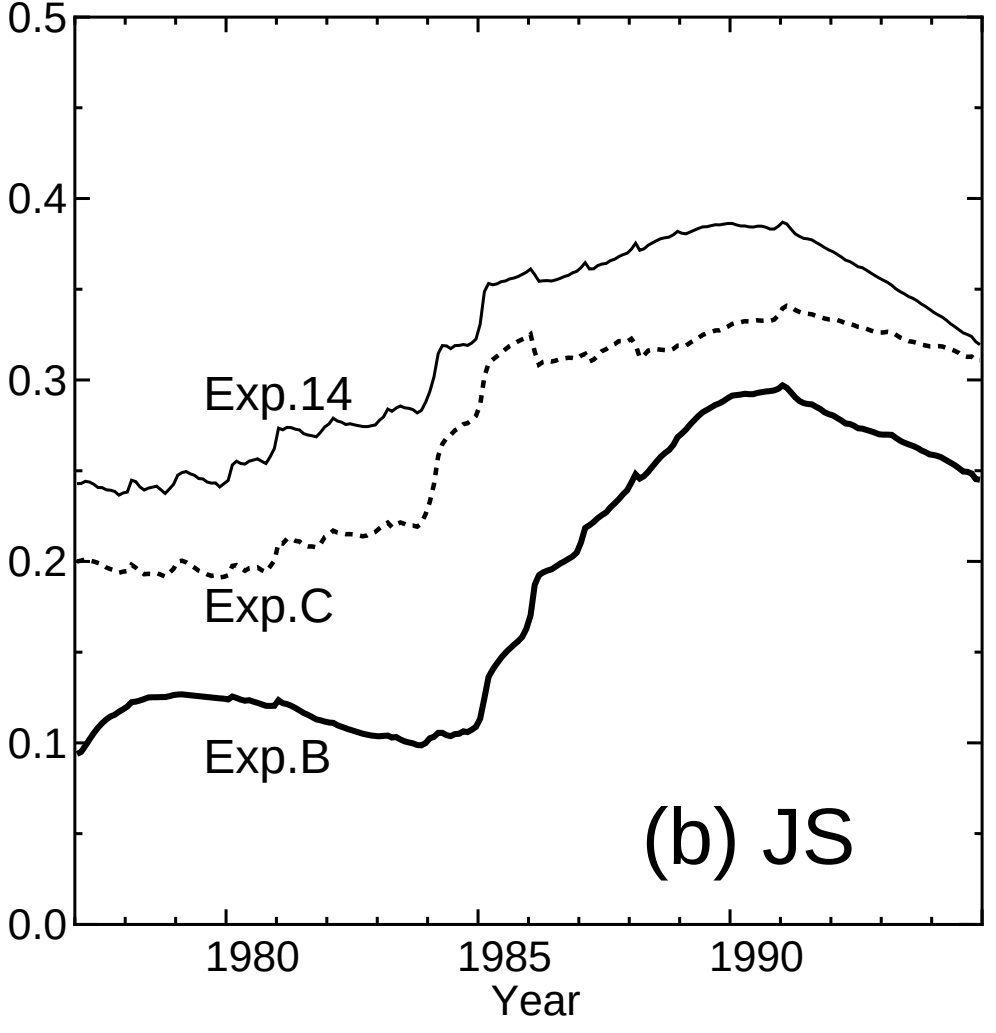
0.5
0.4
0.3
0.2
0.1
0.0
Exp.14
Exp.C
Exp.B
(b) JS
1980
1985
1990
Year

Fig. 8

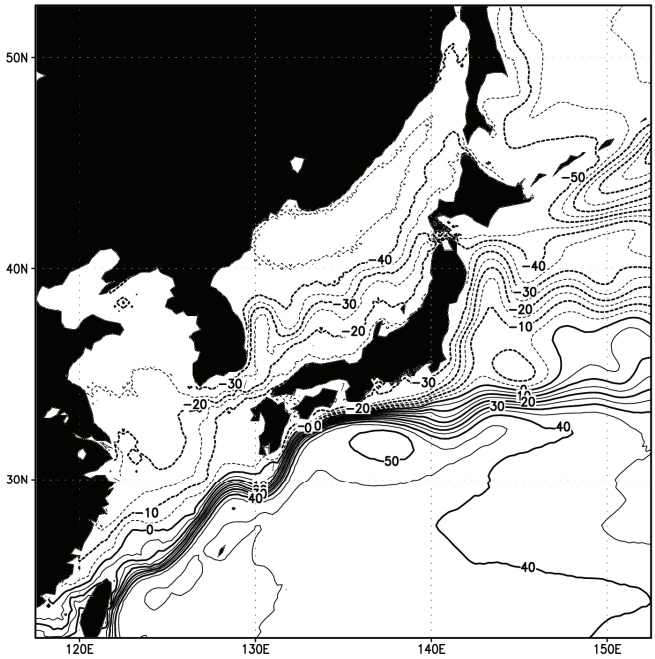

Fig. 9

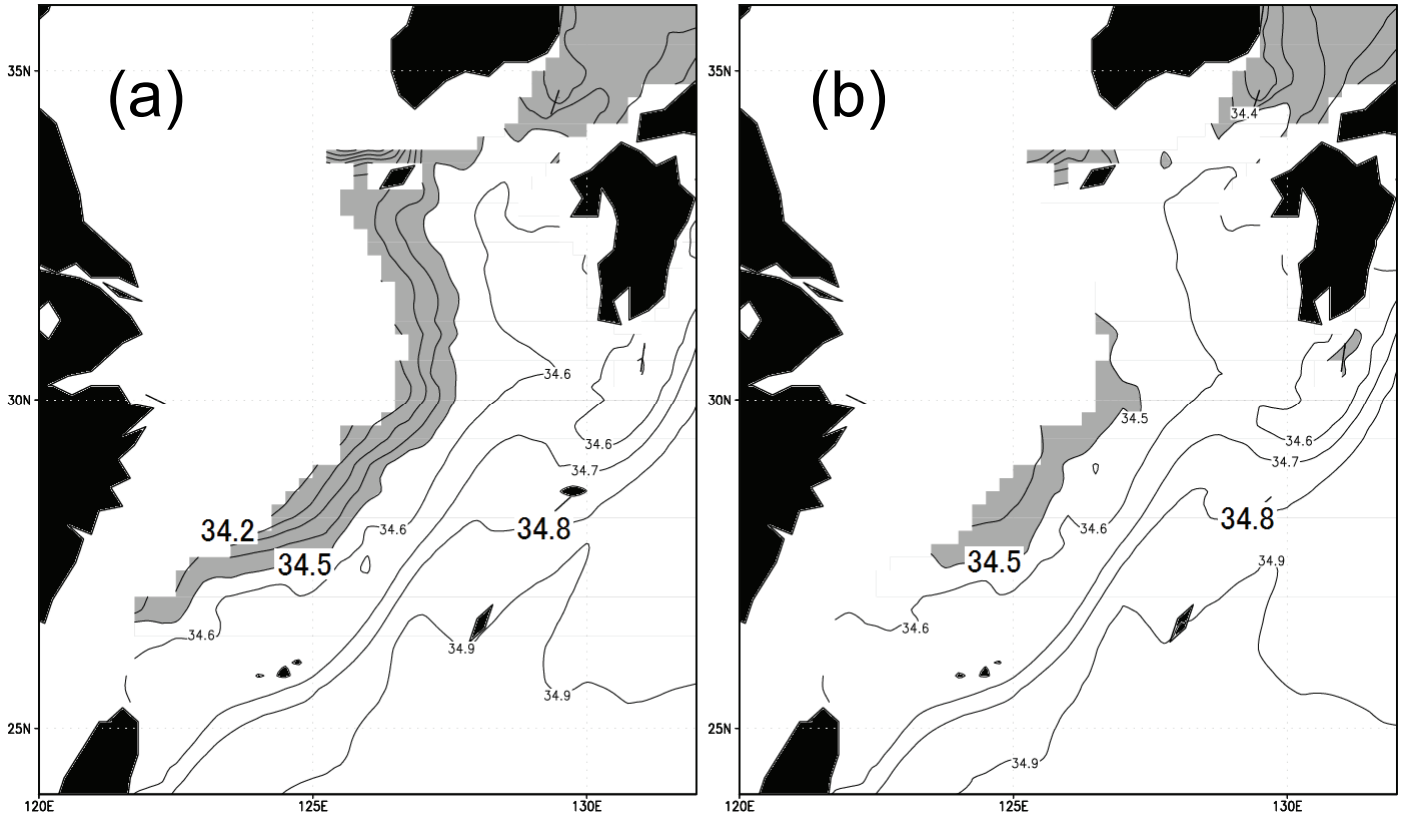

Fig. 10

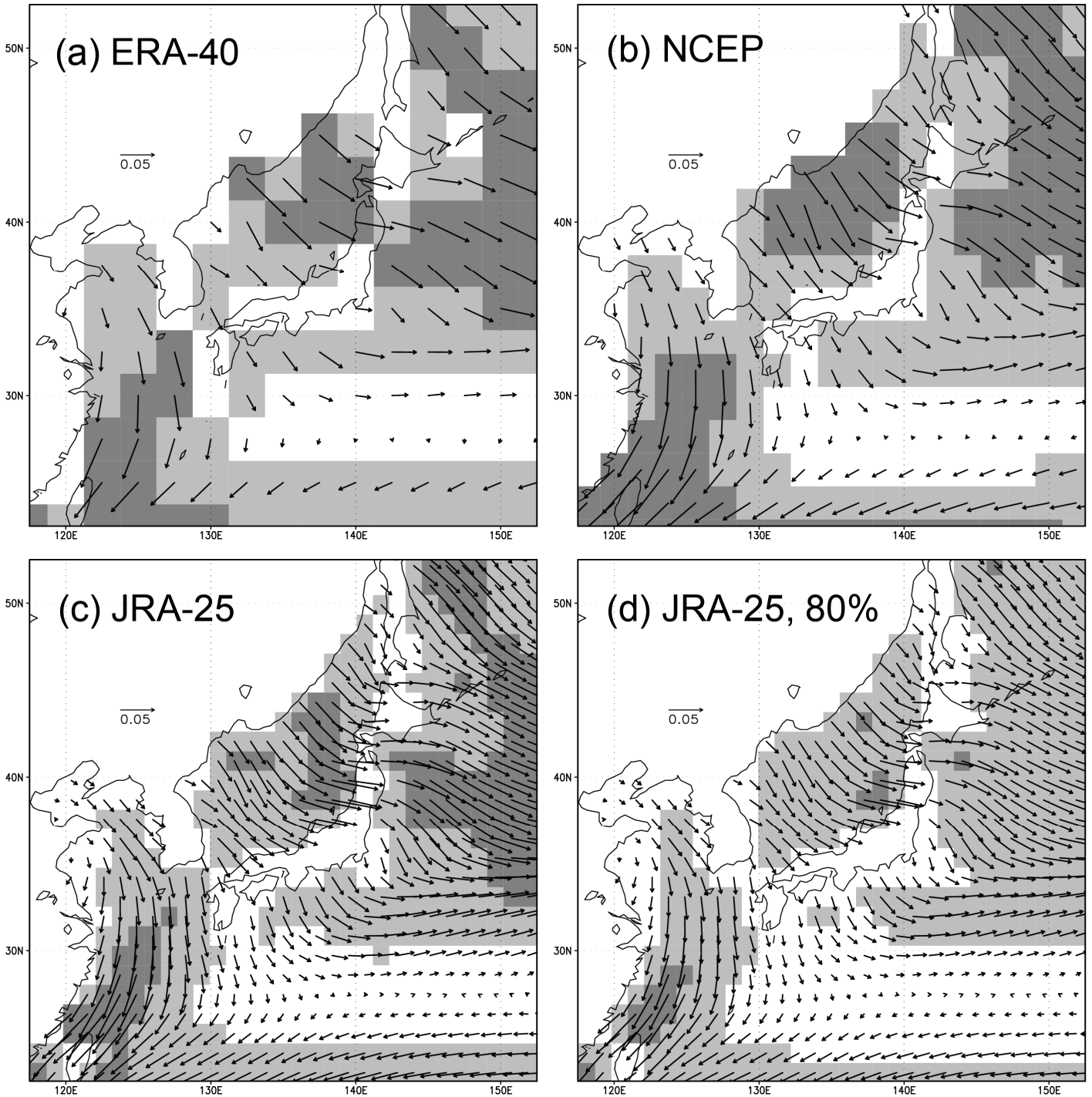
(a) ERA-40
(b) NCEP
(c) JRA-25
(d) JRA-25, 80%
0.05
50N
40N
30N
120E
130E
140E
150E

Fig. 11